COMMUNICATION

Reconfigurable double-sided smart textile circuit with liquid metal†

Chanho Jeong, [ab] Ki Yoon Kwon, [b] Di Wu, [c] Yibo Fu, [c] Yeong-sinn Ye, [b] Sang Gil Lee, [d] Beomchan Kang, [a] Lining Yao, [iD][e] Tae-il Kim [iD] *[b] and Carmel Majidi [iD] *[a]

Smart textiles have emerged as a promising alternative to printed circuit boards (PCBs) for electronics that are flexible, lightweight, and stretchable. However, many existing solutions fall short of providing sufficient electrical properties or are limited to single-sided circuit designs, significantly reducing their utility. In this study, we present a smart textile based on liquid metal and silver flakes that allows for double-sided circuit configurations without the need for *via* holes, offering advantages beyond conventional PCB technologies. This approach allows users to insulate or connect top and bottom circuits as needed, even when the circuits overlap or intersect. The inherent properties of liquid metal facilitate pressure-induced sintering, working in synergy with textiles to provide users with the ability to dynamically alter circuits. This unique feature enables real-time customization, allowing for the addition, removal, or replacement of circuits through straightforward cutting and stitching processes. Demonstrating these characteristics, we showcase diverse applications, including a wristband with a replaceable LED indicator circuit, a reversible teddy bear cloth with two distinct functions, and a customizable DIY heating glove. This double-sided textile circuit that is patterned with pressure-controlled drawing offers new possibilities for multifunctional wearable electronics, bridging the gap between traditional PCBs and flexible smart textiles.

New concepts

In this study, we introduce a reconfigurable double-sided smart textile circuit utilizing liquid metal (LM) and silver flakes (SF), enabling dynamic circuit modifications without the need for *via* holes. While previous double-sided textile circuits and convential printed circuit board (PCB) have required vias or complex fabrication steps to achieve inter-layer connectivity, our approach leverages the porous nature of textiles to enable controlled inter-layer connections through pressure-induced sintering, simplifying fabrication while maintaining flexibility and reconfigurability. This novel mechanism allows for bidirectional interconnections that can be selectively formed or insulated, offering a customizable circuit platform where users can modify, remove, or expand circuits as needed. The ability to reconfigure circuits using simple mechanical operations such as cutting and stitching introduces a new fabrication paradigm for wearable electronics. Demonstrated through applications like a customizable light-emtting diode (LED) wristband, a reversible textile circuit for interactive garments, and a DIY modifiable heating glove, this innovation bridges the gap between rigid electronics and flexible smart textiles, opening new possibilities for multifunctional, reconfigurable electronic textiles.

1. Introduction

The circuit board is the foundation of any electronic device, connecting electro-components and facilitating the transit of electrons across the board to enable functionality. For hard

cased computing systems and devices, printed circuit boards (PCBs) are widely used due to their high accuracy and robustness. In the case of wearable electronics, displays, and devices with slim form factors, flexible printed circuit boards (FPCBs), whose substrates are primarily polyimide (PI), are increasingly being used. However, the rapidly advancing field of human-computer interaction calls for greater flexibility and circuit integration to accommodate smaller, lightweight devices, with additional applications extending to soft robotics, wearable computing, wearable biomedical interfaces, and more.[1–6] When used in these application domains, the limited flexibility, difficulty in modification, mechanical mismatch with the human body, and potential damage and discomfort of FPCBs can result in mechanical failure and user inconvenience.[7–10] Consequently, there is a need to develop novel circuit boards that enhance flexibility and adaptability without sacrificing the electronic functionality of traditional circuit boards.

[a] Department of Mechanical Engineering, Carnegie Mellon University, Pittsburgh, PA 15213, USA. E-mail: cmajidi@andrew.cmu.edu

[b] School of Chemical Engineering, Sungkyunkwan University (SKKU), Suwon 16419, Republic of Korea. E-mail: taeilkim@skku.edu

[c] Human-Computer Interaction Institute, Carnegie Mellon University, Pittsburgh, PA 15213, USA

[d] Department of Semiconductor and Display Engineering, Sungkyunkwan University (SKKU), Suwon, 16419, Republic of Korea

[e] Mechanical Engineering, University of California, Berkeley, CA 94720, USA

† Electronic supplementary information (ESI) available. See DOI: https://doi.org/10.1039/d5mh00462d

As an alternative to FPCB technologies, researchers have developed highly flexible and thin electronics using wavy structures,[11,12] kirigami,[13–15] fabrics,[16–19] or porous elastomers.[20–22] Notably, a serpentine design helps prevent circuit disconnection under extreme stretching and bending.[23,24] Another approach involves using conductive composites,[25–27] with nozzle printing as a common technique for depositing conductive material onto the substrate.[28–33] Liquid metal (LM) has also become a promising material for the circuits due to its electrical robustness and the feasibility of creating channels or percolating networks of conductive fluid.[30,34–45] When integrated into textiles, LM can overcome the shortcomings of traditional FPCBs by providing superior flexibility and ease of modification, essential for wearable technology. However, previous methods primarily focused on single-sided circuit designs, which limit the complexity of circuit configurations.[46] Also, LM droplets embedded in soft materials like polydimethylsiloxane (PDMS) cannot be easily patterned with mechanical sintering since the soft PDMS redistributes pressure away from the droplets.

In this study, we introduce a double-sided smart textile circuit composed of microdroplets of eutectic gallium–indium (EGaIn) LM alloy and silver flakes (SF) embedded within a nonwoven fabric. This double-sided smart textile circuit enables dynamic interconnections between the top and bottom layers without requiring *via* holes, significantly expanding circuit design possibilities. The fabric-based architecture with LM allows users to selectively connect or insulate overlapping circuits, offering unprecedented control over electrical pathways. For example, unlike previous LM-textile applications, which primarily need extra processing steps for insulation or are composed of multiple substrates, our method leverages the porous nature of textiles to facilitate double-sided circuit configurations internal vias. Such functionality allows for highly complex and versatile circuit configurations, similar to multi-layer PCB, that go beyond the constraints of single-layer designs. By leveraging the inherent properties of textiles and liquid metal, this innovation bridges the gap between flexibility and multi-layered electronic integration, opening new possibilities for applications requiring dense, multifunctional circuit layouts.

The conductive textile circuits are formed through pressure-induced sintering, allowing users to modify circuits dynamically. The electrical conductivity of the sintered LM with silver flakes reaches 3.14×10^5 S m^{-1}, demonstrating high-performance electrical interconnects that is suitable for wearable and flexible electronics. The silver flakes (SF) are utilized to enhance the physical and electrical properties of the conductive traces, thereby providing better performance compared to previous LM textile applications.

Fig. 1a presents the schematic of our flexible smart textile, illustrating that circuits can be independently designed on either the top or bottom layer, with the ability to connect (yellow dashed circle and arrows) or insulate (green dashed circle and arrows) them even when their paths intersect. Fig. 1b depicts the actual smart textile with mounted electro-components, showcasing the flexibility and mechanical robustness of the textile substrate. As the substrate is textile, it is flexible enough

to be twisted. This approach to smart textiles with liquid metal is distinct from past methods. Previous research has primarily focused on coating surfaces with liquid metal or embedding liquid metal within textile fibers to achieve conductivity.[18,38,40,41] These methods, while innovative, often resulted in limitations such as single-sided circuit designs or challenges in maintaining robust electrical connections under mechanical deformation. For example, some studies have involved injecting liquid metal into fibers, providing a degree of flexibility and conductivity, but still facing issues with complex processing and limited reconfigurability.[47,48] Our work introduces a unique double-sided circuit design without the need for *via* holes, leveraging the synergy between liquid metal and silver flakes to facilitate selective inter-layer connections by pressure-induced sintering. This allows for dynamic reconfiguration and high conductivity, offering a more versatile and robust solution compared to previous LM-filled fabric technologies. Additionally, our method supports the integration of various types of connectors and the ability to easily modify or repair circuits through simple cutting and stitching, enhancing the practicality and applicability of smart textiles in real-world scenarios.

2. Results and discussion

The smart textile is composed of a TX1109 (Texwipe) nonwoven cloth composed of cellulose and polyester embedded with a dispersion of silver microflakes (SF 94, Ames Goldsmith) and microscale droplets of liquid metal (LM). In its original state, the fabric is electrical insulating, with no percolating network formed among the embedded metal particles. When highly localized pressure is applied, the LM droplets rupture and an electrically conductive pathway is formed.

2.1. Configurable liquid metal circuit design in smart textiles

Scanning electron microscope (SEM) images in Fig. 1c and d show the morphology of the fabric before and after pressure is applied. In the initial state, the fabric surface is coated entirely with liquid metal (LM) particles and silver flakes (SF), with sizes ranging from hundreds of nm to a few μm. Each LM particle has a thin oxidized layer, making it non-conductive. Conversely, Fig. 1d shows LM particles in the circuit area that have been mechanically sintered after a localized pressure is applied. In this sintered state, the ruptured LM droplets connect with neighbor SF and LM inclusions to form conductive pathways. The inset *I–V* curves in Fig. 1c and d indicate the changes in conductivity characteristics before and after sintering. Further details on the sintered and non-sintered LM areas are provided in Fig. S1 of the ESI.†

The SEM cross-sectional view in Fig. S2 of the ESI† illustrates the distribution of particles before and after mechanical sintering. Before sintering, the particles are sparsely spread with a coating thickness of approximately 55 μm. Post-sintering, the gaps between the particles close, resulting in a densely connected LM network. Schematic images in Fig. 1e and f depict
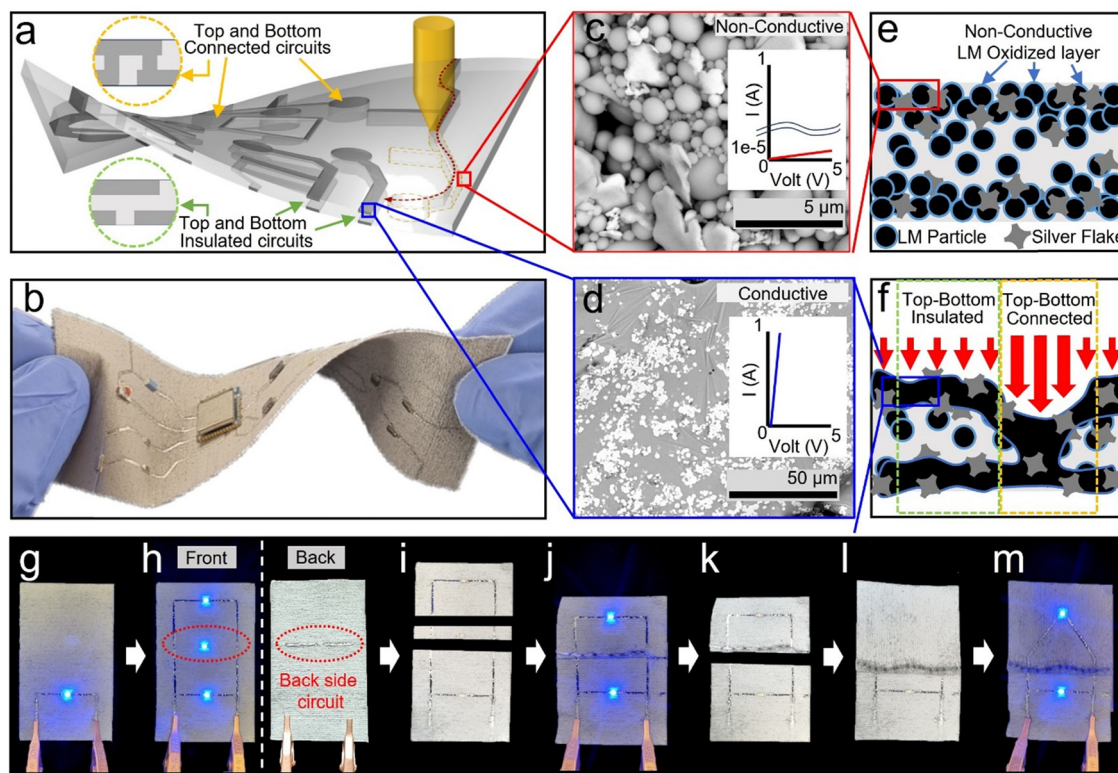
Fig. 1 Conceptualized idea and characteristics of the circuit-modifiable smart textile. (a) A schematic representation of the circuit-designable textile. The circuit can be designed by applying pressure to the surface. (b) A photo image of the flexible circuit-designed textile with diverse components on it. (c) An scanning electron microscope (SEM) image of LM particles and SFs coated on the textile surface, with the inset showing the $I-V$ curve indicating non-conductive behavior. (d) An SEM image of the circuit area formed by pressure. The LM particles are sintered with the embedded SFs, with the inset showing the $I-V$ curve indicating conductive behavior after sintering. (e) The cross-sectional schematic image of the LM particles and SFs on the textile. (f) The cross-sectional schematic image when pressure is applied. Low-pressure (green dashed box) sinters the LM particles existing on the surface while high-pressure (yellow dashed box) sinters the LM through the textile. (g)–(m) Various modifications are possible for the textile circuit. (g) From a simple LED circuit, (h) an additional circuit can be drawn using either the top or bottom layer. (i) An unnecessary circuit parts can be cut out, and (j) reassembled by stitching. A part of the textile can be fully replaced with a blank textile by (k) cutting, (l) stitching, and (m) being designed as a new circuit.

the LM and SF particles on the textile before and after sintering. They coat the entire surface while retaining their shapes, with some particles penetrating the porous material of the textile. Applying pressure, as shown in Fig. 1f, sinters the LM particles. Under low pressure, as indicated by the green dashed box, only surface particles are sintered, while at high pressure, as shown in the yellow dashed box, the LM droplets penetrate deeper into the fabric and rupture to form *via*-like bridges between the top and bottom surfaces of the sheet. This unique ability to form inter-layer connections through controlled pressure enables dynamic electrical pathways, eliminating the need for *via* holes found in conventional PCBs. Fig. S3 (ESI†) reveals how strong pressure deforms the textile and brings the opposite sides closer, altering LM distribution. In lightly pressed areas (Fig. S3b, red box, ESI†), a sparse layer of LM particles coats the fiber, whereas in strongly pressed areas (Fig. S3c, blue box, ESI†), the particles are sintered and interconnected. Fig. S4, ESI,† provides energy-dispersive X-ray spectroscopy (EDS) images for the LM and SF coated textile, showing all chemical components, including indium (In) and gallium (Ga) from LM, and silver (Ag) from the SF, in both sintered and non-sintered states. Further structural analysis was performed using X-ray

diffraction (XRD) to investigate the phase evolution resulting from the reaction between LM and SF. The XRD pattern (Fig. S5, ESI†) reveals distinct peaks corresponding to Ag, $AgIn_2$, and Ag_9In_4, confirming the formation of Ag–In intermetallic compounds. This indicates that silver from the silver flakes reacts with indium from LM during the sintering process, leading to the formation of stable Ag–In alloys.

Fig. 1g–m illustrates the smart textile's unique modifiability and its ability to support independent or interconnected double-sided circuits. Starting with a simple single light-emitting diode (LED) circuit (Fig. 1g), users can expand the design by drawing additional circuits with pressure (Fig. 1h). Moreover, the design is not confined to the upper layer - *i.e.*, the LED in the middle is powered by a circuit formed on the bottom layer (red dashed circle), demonstrating the inter-layer connectivity. To remove an unneeded circuit part, we can simply cut it out (Fig. 1i) and stitch the ends together (Fig. 1j). For a complete redesign, parts of the circuit are removed (Fig. 1k), and a blank textile is stitched in place (Fig. 1l) to allow for new circuit creation (Fig. 1m). By leveraging these characteristics, it is possible to reconfigure previously modified areas and restore the original circuit, although the visual layout may differ from
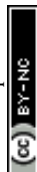
the initial configuration. This level of reconfigurability, combined with the ability to form conductive pathways across textile layers, distinguishes this approach from conventional flexible electronics. To validate the significance of our double-layer approach, we reviewed prior liquid metal-based circuit designs (Table S1, ESI†). While previous studies have demonstrated single-layer circuits,[49–53] double-sided circuit implementations have typically required additional methods, such as *via* hole formations[54] or the deposition of extra insulating layers[55] to prevent unintended connections. In contrast, our approach leverages pressure-controlled sintering to create inter-layer connectivity without the need for *via* holes, enabling a fully reconfigurable and writable textile circuit.

2.2. Fabrication process and the electrical properties of the smart textile circuit

Textiles are essential components of our everyday clothing, offering immense versatility in their applications. Here, we provide more details about our advanced smart textile. Fig. 2a–d details the fabrication process employing a composite textile of 55% cellulose and 45% polyester (Fig. 2a). A solution containing 0.4 g EGaIn and 0.2 g SF in 20 mL isopropyl alcohol (IPA) is sonicated in a 30 mL vial for 3 minutes at 40% amplitude, with a cycle of 3 seconds on and 1 second off. This well-dispersed mixture is then deposited onto an 11 cm × 11 cm textile (TX1109, Texwipe) on a square Petri dish and heated at 75 °C for 20 min to fully evaporate the IPA (Fig. 2b and c). This process is repeated six times, alternating between the front and back sides of the textile, three times each. By applying coatings to both sides, this process ensures that conductive pathways can be formed on both layers of the textile, facilitating the development of double-sided circuits. Following the coating, the bare fibers (Fig. 2a) are transformed into LM particles and SF-coated fibers (Fig. 2c). The final step involves applying pressure to sinter the LM, establishing conductivity in accordance with the circuit design (Fig. 2d). Fig. 2e–h shows the LM and SF coated SEM images depending on the number of coatings and the sintered one. In Fig. 2e, many parts of the fiber remain uncoated, while the three-times-coated fiber in Fig. 2g exhibits uniform coverage. The result after we apply pressure on it is the Fig. 2h. All the LM particles get sintered being connected to each other and the SFs are randomly dispersed within the LM.

Next, we examine the electrical and electromechanical characteristics of our LM circuit on the smart textile. First, we
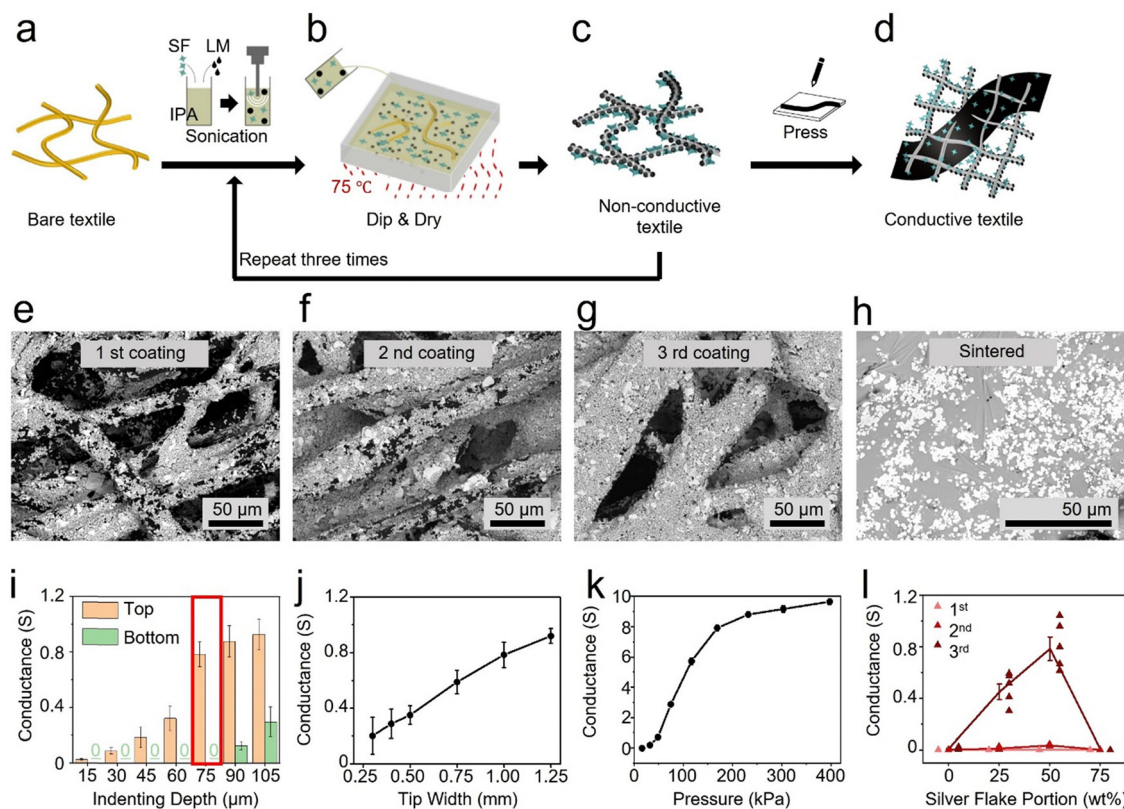

Fig. 2 Basic electrical properties. (a–d) The fabrication process of the circuit-designable smart textile. (a) A clean bare textile. (b) LM and SF sonicated solution is poured on the textile, placed on a 75 °C hot plate to evaporate the solvent. (c) LM particles and SF are evenly coated on the textile. (d) By adding pressure, LM particles get sintered forming a conductive circuit. (e)–(g) SEM images of the LMs particles and SFs coated on textiles for (e) one, (f) two, and (g) three times of coating. (h) The SEM image when the three times coated textile gets sintered by pressure. (i) The conductance depends on the depth of a 1 mm diameter rod. When exceeding 90 μm, the opposite side becomes conductive, losing its bilayer characteristic. (j) A thicker rod generates higher conductance as the circuit width increases. (k) The vertical conductance through the textile depends on the 1 mm diameter rod pressure. (l) The conductance depends on the number of coatings and the SF portion.

measure the electrical conductance as a function of the depth of indentation during mechanical sintering. The overall thickness of the smart textile is approximately 300 μm, and the experiment was performed by indenting with a rigid 1 mm diameter rod while maintaining a constant depth as it was dragged across the textile. In Fig. 2i, the indenting depth was gradually increased by 15 μm increments. Our objective was to identify the depth that yields the highest conductivity without penetrating the opposite side, as we aim to facilitate a double-sided circuit design with controllable interconnections between the layers. As the depth reached up to 105 μm, the conductance continued to increase. However, at 90 μm, the bottom side had already become conductive. Consequently, the optimal indenting depth for achieving the highest conductivity while maintaining electrical insulation between both sides was established at 75 μm under a pressure of 53 kPa, resulting in a conductivity of 3.14×10^5 S m^{-1}. Notably, the insulation between the two sides of the smart textile was preserved even when circuits were designed to overlap at an indenting depth of 75 μm at both sides, ensuring that the two layers function independently unless intentional interconnections are made. As shown in Fig. S3a (ESI†), this insulation is maintained due to the textile's ability to recover unless high pressure applies. Thus, by controlling the pressure depth, circuits on either side of the textile can either remain insulated from each other or be electrically connected, enabling versatile circuit reconfiguration across the textile layers. If a connection between the sides is desired, simply applying a pressure exceeding 200 kPa (Fig. 2k) enables the formation of a reliable conductive. The impact of the rod diameter was also assessed in Fig. 2j. As the rod's diameter increases, the conductance increases, correlating with the increased cross-section area of the circuit. The minimum circuit width that can be fabricated using the rod-drawing method is 0.3 mm (Fig. S6, ESI†). For all subsequent experiments, unless otherwise mentioned, a 1 mm rod was used. Fig. 2k presents measurements for the vertical conductance through the top and bottom layers, where the conductance was measured under varying pressures. As pressure is intensified, the conductance between the layers also increases, demonstrating that mechanical force can be used to dynamically establish or break interconnections. Eventually, conductance is observed to increase and saturate at around 200 kPa, indicating that a stable interlayer connection can be maintained beyond this threshold.

In Fig. 2l, a more precise examination of the data was conducted, reflecting variations in the SF content. The process involved altering SF portions, with conductance measurements taken for each number on both sides coating. Fig. S7 in the ESI† displays the distinct particles formed as the SF portion varied. Initially, when no SF was added, only LM particles were present, and the SF became more pronounced, as its proportion increased. Eventually, when SF constituted 75 wt% of LM, LM particles are significantly less detectable. The 50 wt% ratio, highlighted with the red box, is identified as the optimal ratio for our research. Fig. S8, ESI,† presents SEM images of particle-coated fibers at different conditions. The solution with the SF

portion from 0 wt% to 50 wt% showed quite a reasonable tendency. As the SF portion increases, the fibers are better coated and the number of coatings allow the particles to more completely cover the fibers. SF here works as an anchor to wet to the surrounding LM droplets and hold them in place. Again, the 50% red box is the optimized condition for our research, balancing conductivity and adhesion stability across the textile layers. Interestingly, when the SF reaches 75% of the weight fraction, adhesion with the fibers is dramatically reduced and the coating itself failed. It appears that the coating did not adhere properly from the beginning due to a lack of adhesion. Perhaps this is because a critical amount of liquid metal is required to simultaneously wet to the SF particles and fibers and keep the coating intact.

Fig. S9 in the ESI† presents SEM images of the LM-SF coatings after the mechanical sintering step. Fibers covered by LM-SF coatings with the SF portion from 0 wt% to 50 wt% all appear to show sintering of the LM droplets. However, the relative lack of SF particles results in the presence of void when pressure is applied, especially for the 0 wt% condition. It underscores the necessity of incorporating SF to stabilize the mechanical coating and ensure the uniform sintered area. For the 75 wt% SF coating, there isn't a sufficient concentration of LM particles to coalesce when ruptured. The overall electrical properties for these different cases are shown in Fig. 2l. With a single front and back side coating, the conductance was zero regardless of how much SF was included. The best performance was at 3 times of coating with 50 wt% SF. These results indicate that, while LM alone can achieve partial conductivity through sintering, the inclusion of silver flakes significantly improves the magnitude of conductance. This clearly highlights the critical role of SF in achieving consistent electrical performance under practical conditions. Fig. S10 in the ESI† shows how the conductance changes only depending on the number of coating layers for the 50 wt% SF concentration. Following application of the second coating, coated textile has some conductivity and eventually has adequate conductance following application of the third coating. This number of coating cycles is the result of extensive testing. Even a single coating can yield conductivity if an amount of LM and SF equivalent to that used in three coating cycles is applied, but this approach leads to non-uniform coating and significant variation in conductance across different areas. This is depicted in Fig. S11 (ESI†), where Fig. S11a (ESI†) indicates the measurement points for conductance on the smart textile and Fig. S11b (ESI†) compares a single coating with three separate coatings. A single coating resulted in substantial variability in conductance and high error margins, whereas three coatings produced uniform conductance with lower variability. To further evaluate the practical applicability of the smart textile, we evaluated the electrical stability under real-world conditions with those of commercial FPCBs, including varying temperature, humidity, and pressure (Fig. S12, ESI†). The results demonstrate that our smart textile performs comparably to FPCBs under conditions of 95 °C high temperature, 90% high relative humidity, and atmospheric pressure reduced by −0.02 MPa. The results demonstrate that our textile circuit performs comparably to

FPCBs. Furthermore, Fig. S13 in the ESI† depicts the precision of circuit patterning in our smart textile, demonstrating that adjacent 1 mm width circuits can be positioned as close as 300 μm apart without interference.

To achieve the results presented here, extensive optimization experiments were conducted, including the selection of SF. Since the electrical properties of our double-sided textile circuits depend on the uniformity and connectivity of LM-SF coatings, optimizing the flake size and distribution was critical to achieving stable interconnections between the top and bottom circuits. Fig. S14 and S15 (ESI†) summarize the experimental findings for the smaller SF91 (Ames Goldsmith, average size = 3.22 μm) and the ultimately chosen SF94 (Ames Goldsmith, average size = 5.86 μm), respectively. The SF size disparity between the two flakes is clearly observed in the powder state images of the Fig. S14 and S15 (ESI†), which highlights the smaller dimensions of SF91. In Fig. S8 (ESI†), it was previously observed that while SF facilitates the bonding between LM particles and contributes to fiber coating, its inherent adhesion to the fibers is relatively weak. In terms of coating quality, SF91 exhibited a smoother and visually more uniform coating compared to SF94, demonstrating satisfactory coating even at 75 wt%. This behavior is attributed to the smaller size of SF91, which reduces the contact area between SF and the fibers, thereby minimizing adhesion-related inconsistencies. However, the most uniform and defect-free performance was still achieved at 50 wt% following the sintering process. At 75 wt%, the high density of SF particles continued to hinder fiber adhesion during the pressing process, leading to the detachment of the LM from the fiber. For a direct comparison with SF91, Fig. S15 (ESI†) illustrates the performance of SF94, rearranged from Fig. S7–S9 (ESI†). As shown in Fig. S16 (ESI†), which compares conductance values based on SEM and experimental data, both SF91 and SF94 demonstrated the highest conductivity at 50 wt%. However, SF94 achieved approximately 1.67 times higher conductivity than SF91, which is attributed to the smaller size of SF91 limiting its ability to effectively anchor neighboring LM particles. Based on these results, SF94 was selected as the most suitable material for double-sided circuits.

Furthermore, the impact of sonication time on SF performance was evaluated, as shown in Fig. S17 (ESI†). At 1 minute of sonication, incomplete particle formation resulted in liquid-state clumps (highlighted with yellow circles). At 2 minutes, larger LM particles were observed, leading to uneven coating. Additionally, as shown in the sintered images, the larger LM particles buried SF particles, reducing the area of contact with LM and thereby weakening adhesion. Conversely, a sonication time of 3 minutes yielded well-formed LM particles, achieving uniform coating and strong adhesion, and was therefore identified as the optimal condition.

A further notable merit of our research is the versatility of textiles that can be utilized. Fig. S18 in the ESI† shows the basic conductance data for 100% polyester, cotton, linen, and stretchable knitted cotton. Depending on the textile, the conductive properties may differ and require some further

optimization, but in general, they all have the potential to be compatible with this process as double-sided circuit designs. For instance, linen and knitted cotton showed higher conductivity even better than the nonwoven textile composed of 55 wt% cellulose and 45 wt% polyester used in this research. However, this is only true after they were coated 6 times. Fig. S19 in the ESI† displays SEM images of various textiles after coating. These findings confirm that our approach is compatible with multiple textile substrates, enabling the design of high-density, multifunctional double-sided circuits for a range of wearable electronic applications.

2.3. Demonstration in a wearable device

The pressure-controlled, writeable nature of the smart textile presented here allows users to directly design their own circuit either by hand or using a motorized stylus. After the circuit is patterned, it is important to be able to protect the circuit from unintended pressure that may generate additional conductive pathways. Such pressure-induced sintering may result not only from external indenting forces but also from mechanical deformations inherent to the dynamic environment of smart textiles, as demonstrated in Fig. S20 (ESI†). Fig. S20a–d (ESI†) present SEM images of the circuit subjected to bending, folding, torsion, and stretching, respectively. Significant change was not observed under bending with a radius of 2.5 mm (Fig. S20a, ESI†). In contrast, folding caused local compression of the LM and mechanical failure, leading to significant sintering (Fig. S20b, ESI†). Torsional deformation resulted in the formation of small, scattered sintered clusters over a broad area (Fig. S20c, ESI†). Furthermore, stretching by 20% induced severe and continuous sintering across the circuit (Fig. S20d, ESI†). Notably, in the stretching test, stretchable knitted cotton was employed instead of nonwoven fabric to accommodate the applied strain. To address these challenges, we introduce two distinct methods for circuit protection. One method fully protects the circuit, enabling any further LM sintering, and the other provides some protection but still allows for modifications under high pressure. For both methods, circuit-designed textiles are passivated by PDMS in different ways.

To fully protect the circuit, the textile is coated with PDMS and left at room temperature for 4 h, allowing the PDMS to penetrate the porous textile before curing at 80 °C. As shown in Fig. 3a, no matter how hard we try to connect the disconnected LED circuit, the circuit remains fully protected, preventing further sintering. For the semi-protected circuit shown in Fig. 3b, the PDMS protects the circuit but the user can still further draw on the circuit. The difference arises from the absence of a waiting period before the PDMS curing. The LM particles underneath the PDMS still have the freedom to be connected. Video S1 in the ESI† clearly shows the difference. After coating with a PDMS semi-protection layer, the pressure-conductance data for additional circuit designs is presented in Fig. S21 (ESI†). Although the conductance is approximately 0.54 S, which is lower than the 0.78 S observed without the protection layer, it remains sufficient for circuit operation. Moreover, this PDMS protection layer prevents particle detachment

when in a bare state (as shown in Fig. S22, ESI†) and significantly enhances overall durability (as demonstrated in Fig. S23, ESI†). Fig. S22a (ESI†) highlights the degree of particle detachment observed after four repeated tape tests. The corresponding relative resistance changes are shown in Fig. S22b (ESI†). Notably, after the first peeling cycle, the circuit maintained stable resistance values even during subsequent tape tests. Durability testing through 10 000 cyclic bending tests is presented in Fig. S23 (ESI†), where Fig. S23a and b (ESI†) depict the bending conditions with a maximum diameter of 2.5 cm in the released state and a minimum diameter of 0.5 cm in the bent state, respectively. The results in Fig. S23c (ESI†) show resistance change with 10 000 bending of the smart textile with a protection layer. It was because PDMS encapsulation reduced mechanical stress in the electrode

and maintained uniform resistance without significant variation, while the bare textile exhibited an initial sharp increase in resistance during the early cycles, followed by a gradual yet consistent upward trend over time. Building upon the mechanical reliability conferred by PDMS encapsulation, we further demonstrate the electrical stability of the sensor under various modes of mechanical deformation. As shown in Fig. 3c–f, the relative resistance changes by bending, folding, torsion, and stretching were measured. In the case of bending, the resistance variation remained within 1.5% at a curvature of 4 cm^{-1} in both directions (Fig. 3c). Despite folding with a radius below 500 μm being a highly critical deformation, the sensor exhibited stable performance with resistance changes confined within 25% (Fig. 3d). Under bidirectional 180° torsional deformation, the sensor
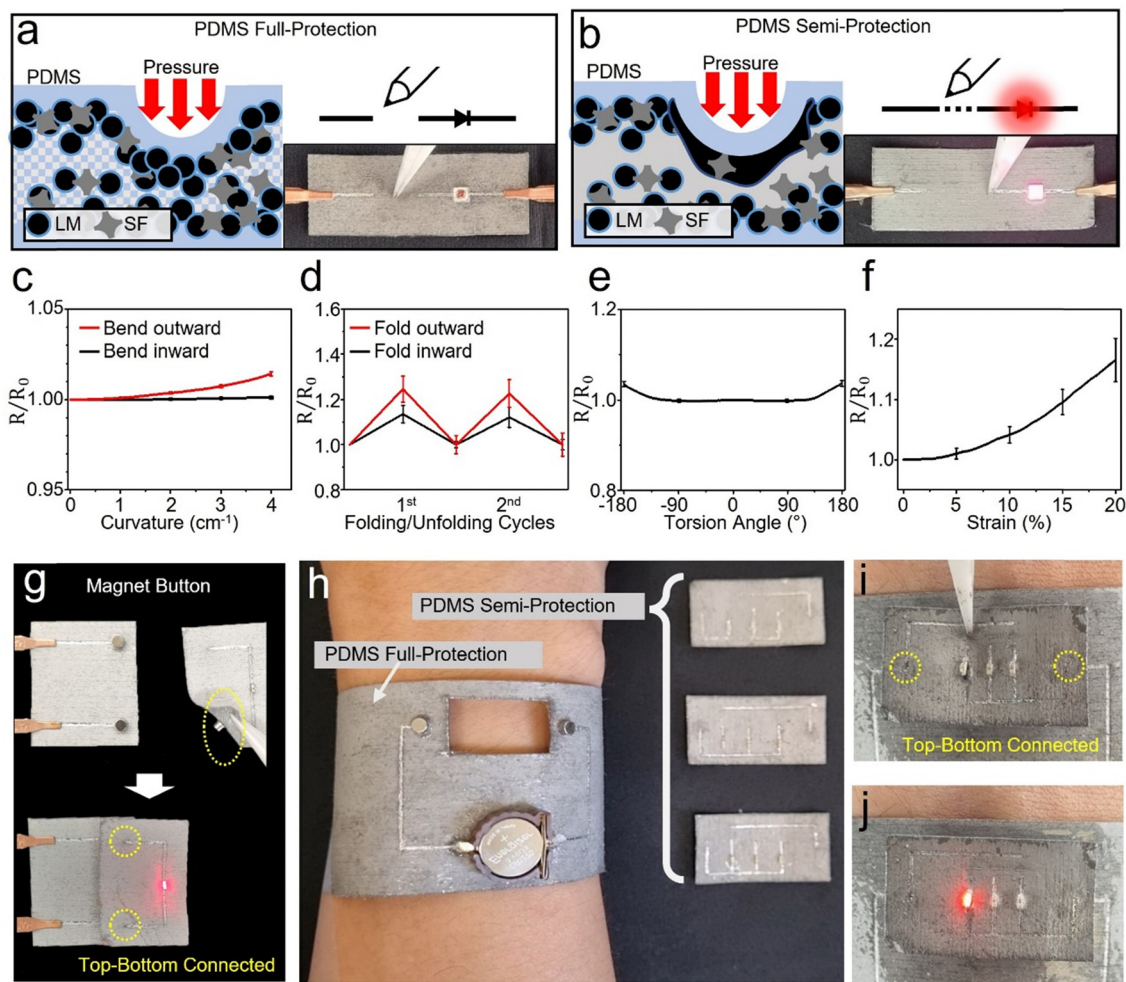

Fig. 3 Encapsulation strategies for circuit protection. PDMS, as a protecting layer, exhibits different abilities based on the coating method. (a) PDMS permeates the entire circuit-designed textile, fixing all the circuits. Additional pressure can not sinter further LM particles protecting the existing circuit. (b) PDMS covering only the surface protects the circuit and allows further LM particles to be sintered at higher pressure. A disconnected circuit can still be modified and reconnected with high pressure. (c)–(f) Relative resistance changes of the PDMS-protection circuit under various mechanical deformations. (c) Bending-induced resistance changes depending on the bending direction. (d) Resistance changes after the first and second folding/unfolding cycles with a radius below 500 μm. (e) Resistance changes during torsion from −180° to 180°. (f) Resistance behavior under tensile strain up to 15%, using the previously introduced stretchable textile. (g) Textiles with circuits can be designed as separated parts and connected by conductive buttons. (h)–(j) A wristband with adjustable indicator LEDs. (h) The wristband is covered by the full-protection PDMS layer, while the replaceable LED indicators part is semi-protected by PDMS. (i) The LED part attaches to the wristband with the magnet buttons, and (j) applied pressure turns on the selected LED by connecting the circuit.

showed a relative resistance change of 3.7%, as shown in Fig. 3e. The experimental setup for this test is detailed in Fig. S24, ESI.† In the stretching test, the sensor was subjected to a tensile strain of 15%, during which the relative resistance change was recorded as 9% (Fig. 3f). The stretchable smart textile used for this test, introduced previously in Fig. S18d (ESI†), was composed of knitted cotton. Its mechanical characteristics, including a non-linear strain–stress profile and a maximum stretchability of 34% before fiber failure, are provided in Fig. S25 of the ESI.†

An inherent advantage of our smart textile is that, by primarily relying on liquid metal as the conductor, it preserves the mechanical compliance and versatility of the host textile. Using conductive buttons, two separate parts can be easily connected and disconnected. Fig. 3g is a simple LED circuit with conductive magnet buttons, allowing the LED to illuminate upon connection. This characteristic extends to other conductive connectors like snap buttons and conductive Velcro as shown in Fig. S26, ESI.† Notably, as indicated by the yellow dotted circle, the magnet button is attached to the opposite side of the LED circuit, confirming the utilization of the top-bottom connection functionality.

Combining the above two characteristics, we created a customizable wrist LED indicator, as shown in Fig. 3h. The wristband is composed of a power source and magnet button connectors covered by a fully protective PDMS layer. Attachable indicators with disconnected LEDs are prepared and passivated by the PDMS semi-protective layer. Fig. 3i and j demonstrates

the functionality of this wrist indicator. On the user's demand, the user only needs to connect the circuit using a sharp tool while the attachable indicator is loaded on the wrist, and it can be easily replaced. Once again, the conductive magnet button is strategically positioned on opposite sides of the textile utilizing the top-bottom connection, thereby improving the design and simplifying the circuit layout. Although LED indicators were used in this demonstration, the versatility extends to showcasing various functions based on the specific circuit design as seen in the next two applications.

2.4. Functional demonstrations: teddy bear cloth and DIY heating glove

With our LM/SF-based smart textile, we made a reversible teddy bear cloth that has different functions on each side, highlighting the independent circuit configuration in each layer. Referring to Fig. 4a, the red side functions as a cloth with an LED activated in the dark, facilitated by a photodetector acting as a switch. Referring to Fig. 4b, the opposite green side operates as a heating cloth when buttoned up. Both circuit sides have magnet buttons to connect to a 3.7 V lithium-polymer (LiPo) battery, as illustrated in the overall circuit diagram in Fig. 4c. Despite the crossing of circuits on both sides (indicated by the green dashed circle), they remain well-insulated and fully operational. In Fig. 4d and e, we placed the cloth onto a teddy bear and checked the functionality of the circuit. The LED activates automatically in a dark place
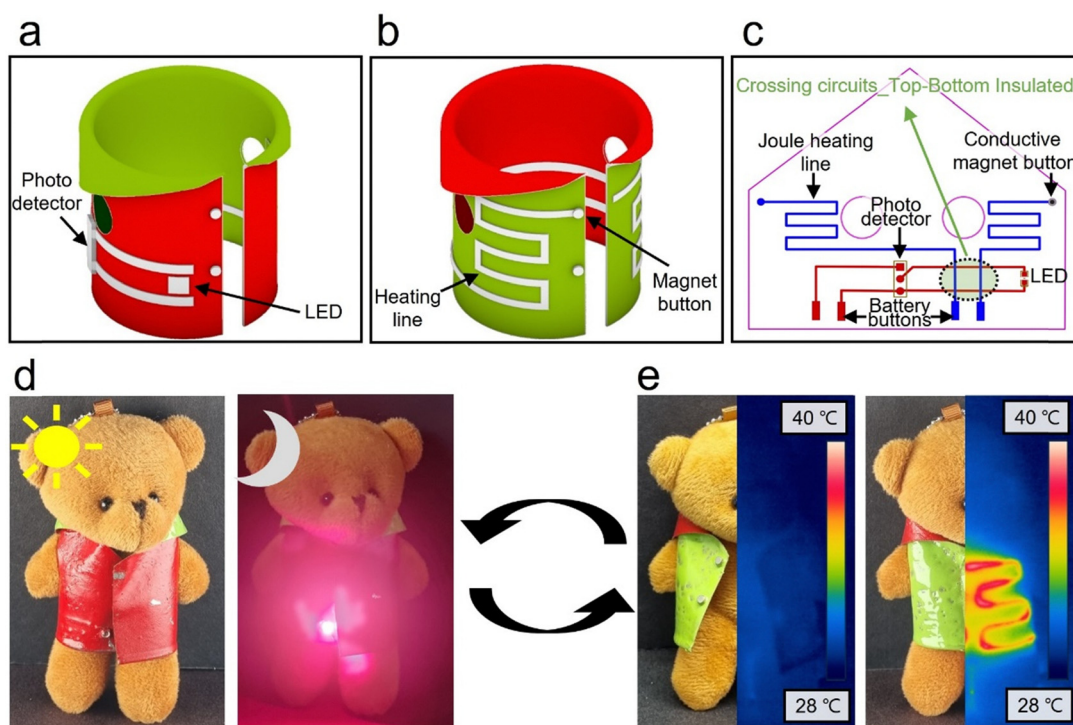

Fig. 4 Reversible cloth with two different functions. (a) A schematic of one side of the cloth with an LED and a photodetector. (b) The schematic of the reversed version with the Joule heating system. (c) The circuit design on both sides of the cloth. The section where the circuits cross while maintaining insulation is indicated by the green dashed circle. (d) A teddy bear with LED cloth. The LED turns on when the surroundings darken. (e) The teddy bear after reversing the cloth. The Joule heating system operates when the cloth is buttoned up.

(Fig. 4d). If we flip the cloth and place it on the opposite side, the cloth can be used for heating. As we can see in Fig. 4e, before the smart garment is buttoned up, the heating circuit is disconnected and does not undergo Joule heating. However, once we button up, the magnet buttons connect the circuit and the garment generates heat of up to 40 °C. This dual-functionality is enabled by the double-sided circuit configuration, allowing independent circuits to coexist without interference. For unobtrusive audiovisual materials, the teddy bear demonstration without the colored version is in Fig. S27 of the ESI.† The demonstration of cloth flipping and the battery connection is shown in Video S2 of the ESI.†

Combining the circuit-modifiable characteristics with a heating system provides the ability to control the heating area according to user preferences. Fig. 5a is a simple serpentine circuit with a temperature map taken by an infrared (IR) camera. Applying 2 V to the circuit generates heat of up to 40 °C. Subsequently, we modify the circuit by creating an internal electrical short (Fig. 5b). As the current tends to flow along the path of least resistance, the heating area also shifts to where the current flows. This phenomenon is shown starting from powering on in Video S3 of the ESI.† Fig. 5c illustrates the conceptualized DIY heating glove with three distinct sections capable of generating heat independently. Its operation is controlled by a connected remote-operating microcontroller unit (MCU). Moreover, if the user applies pressure to create a short circuit, the heating area can be altered, as demonstrated in Fig. 5a and b. The real DIY heating glove we made is shown in Fig. 5d with the circuit diagram. The MCU's three different outputs can be wirelessly powered by a smartphone. Since the
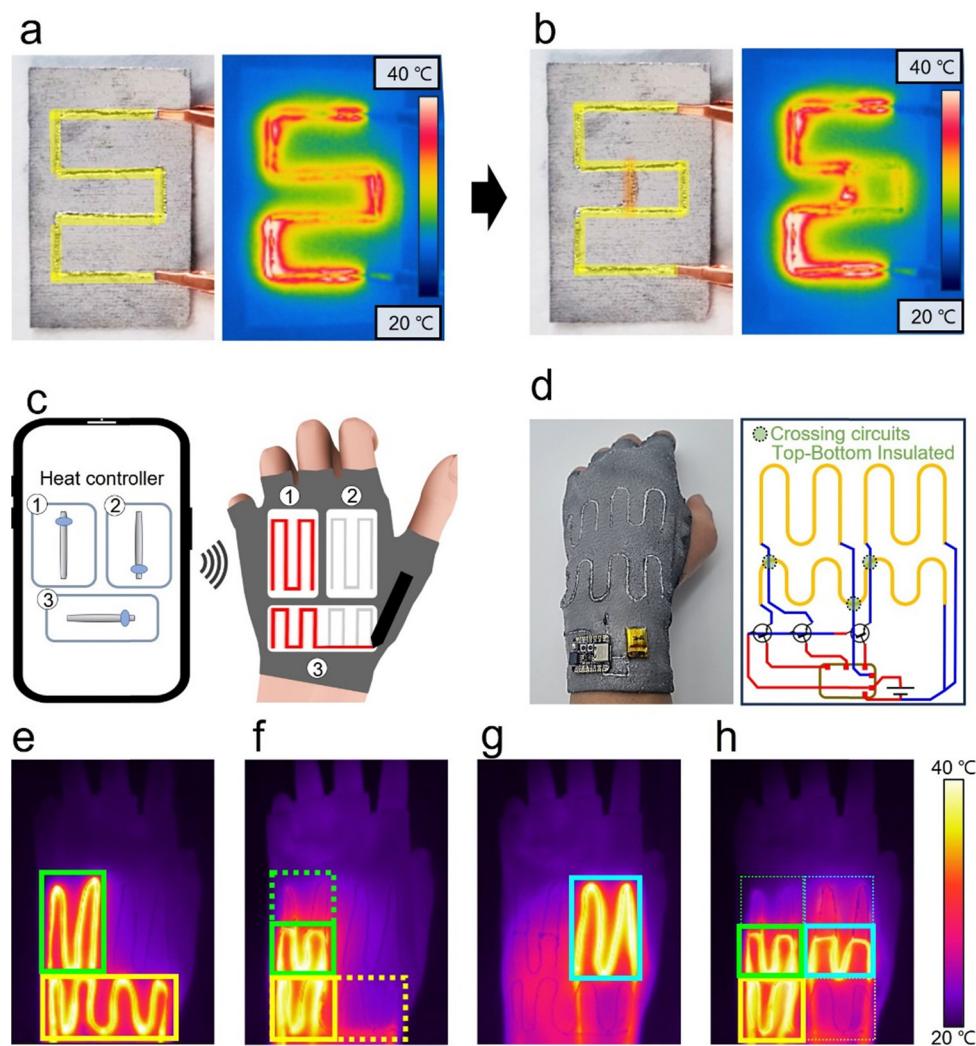

Fig. 5 Customer DIY heating glove. (a) Joule heating on the smart textile with the circuit pathway is highlighted in yellow. (b) Drawing an additional circuit, highlighted in orange, changes the current flow direction, consequently altering the heating area. (c) and (d) A DIY glove with adjustable heating zones. (c) Schematic image illustrating the operating mechanism. It allows users to control the heating intensity in three zones through a smartphone, and additional circuitry on the gloves enables more precise heating area adjustments. (d) Actual wearing image of the gloves and a circuit diagram. In the green dashed circle, the circuits cross while maintaining insulation from each other. (e)–(h) Infrared images of the heating area are adjusted by the user. (e) Areas 1 and 3 are activated. (f) Areas 1 and 3 have their heating areas changed through additional modifications. (g) Only area 2 is activated. (h) Area 2 is also modified, and the adjusted areas 1, 2, and 3 are all activated.

MCU regulates the current to be below 600 mA, which is insufficient for Joule heating, it controls the transistors connected to each output. Depending on the user's command, the MCU-controlled transistors determine whether to allow the flow of current from the 3.7 V LiPo battery. Notably, the circuit connecting area 1 and area 2 passes through the bottom side of area 3, which performs Joule heating as they are insulated. This insulation prevents unintentional activation through heating, ensuring that each heating zone operates independently. Without proper layer insulation, current leakage would disrupt circuit functionality, rendering the entire system ineffective. Fig. 5e–h presents the user-controlled heating map. Fig. 5e displays the temperature distribution when areas 1, green box, and 3, yellow box, are activated. In Fig. 5f, the user modified the heating area to a smaller region for areas 1 and 3 in the dot-square areas. Fig. 5g illustrates only area 2 in operation, and with further user modification to area 2 and operating all the areas, it eventually becomes like Fig. 5h. In real-world scenarios, individuals with poor peripheral circulation may require localized heating at the fingertips, whereas those engaged in outdoor labor or undergoing rehabilitation may prefer warmth around the wrist or knuckles. By physically modifying the circuit, users can tailor the system to their specific needs, thereby demonstrating the reconfigurable and user-adaptive capabilities of the proposed textile platform. Moreover, this application is not confined to simple thermal control but serves as a representative example of how the system can accommodate diverse, user-driven functional demands.

3. Conclusions

In summary, we developed an LM particles and SF-based circuit-modifiable smart textile. Initially, LM particles are non-conductive as they are surrounded by an oxidized layer. However, once they rupture and coalesce, the LM droplets combine with the SF particles to form conductive pathways. Using this phenomenon, the circuit can be manually designed by simply adding pressure to the textile.

One of the important strengths of our approach is the fact that it can be designed as a double-sided circuit, which many recent efforts in soft electronics often overlook. Combining the characteristics of porosity in textiles and the liquid state of LM allows for connection between the top and bottom layer without making a *via* hole, or alternatively, keeping it insulated by controlling the pressure. This controllable inter-layer connectivity is a key advantage over traditional textile circuits, allowing dynamic circuit modifications in a simple and accessible manner. Furthermore, considering that the substrate is a textile, we could leverage all the benefits that textiles offer and showcase several unique characteristics. It could be cut to remove unnecessary parts and reconnected by stitching or can be fully replaced with a blank textile to redesign the circuit. In addition, various types of conductive connectors such as snap buttons, magnets, or conductive Velcro can be used to connect and disconnect diverse separated parts.

In addition to pressure-controlled circuit patterning, we also introduce a passivation method to seal the circuit and prevent the inadvertent formation of additional conductive pathways. If we allow the PDMS to penetrate the textile, it fully protects the circuit and shields it from further mechanical sintering. On the other hand, if we cure the PDMS before it penetrates, it somehow protects the circuit from unexpected low pressure but can still further design the circuit with high pressure. With all the introduced features, we demonstrate a wristband that has a replaceable LED indicator circuit, a reversible teddy bear cloth that has two different functions such as lighting up at night and heating when buttoned up, and a customer DIY heating glove that heating area can be modified by the users. These demonstrations highlight the versatility of our double-layer circuit design, showing how circuits on both sides of the textile can function independently or be selectively connected when needed. The ability to integrate multiple functionalities into a single fabric structure without *via* holes provides new possibilities for dynamic and reconfigurable electronic textiles.

While our approach to smart textiles with liquid metal offers significant advancements, it is not without limitations. One of the primary concerns is the biocompatibility of the materials used. Liquid metals like gallium and its alloys need thorough evaluation to ensure they are safe for prolonged skin contact or potential use in medical implants. Current studies indicate that gallium and its alloys are generally safe, but comprehensive toxicological assessments are still required to fully understand their interactions with living organisms.[56] Future research should focus on assessing the biocompatibility and long-term stability of these materials. Additionally, given our method's capability for double-sided circuit designs, further exploration into fabric stacking for multi-layer circuits could enable more complex and sophisticated circuit configurations. Further studies on large-scale manufacturing processes and durability under various environmental conditions are also essential to bring this innovative technology from the lab to real-world applications.

4. Experimental section/methods

4.1. Fabrication of circuit-designable smart textile

A solution containing 0.4 g of EGaIn, 0.2 g of SF, and 20 mL of IPA was initially prepared in a 30 mL vial. Using a tip sonication (Sonics & Materials, Inc., USA), the solution was sonicated for 3 min at 40% amplitude, with cycles of 3 s on and 1 s off. Subsequently, the prepared solution was gently poured onto an 11 cm × 11 cm textile (TX 1109, Texwipe, USA) consisting of 55% cellulose and 45% polyester, which was laid on a square Petri dish. The coated textile was then subjected to heating at 75 °C for 20 minutes to ensure complete evaporation of the IPA solvent. This coating process was iterated six times on both the front and back sides of the textile, with three coatings applied to each side. Finally, pressure was applied to the coated textile to sinter the LM particles, thereby creating conductivity pathways following the desired circuit design.
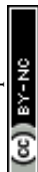
4.2. Scanning electron microscopy (SEM) imaging

Scanning electron microscopy (SEM Mira 300) imaging was conducted to examine the surface morphology of the LM and SF coatings on textiles, as well as to assess the differences resulting from varying ratios of LM to SF, coating cycles, and the type of textile. For the observation of cross-sectional surfaces, samples were prepared by freezing them in liquid nitrogen for 5 minutes to achieve a brittle state, followed by fracturing using scissors.

4.3. X-ray diffraction (XRD) analysis

X-ray diffraction (Smartlab, Rigaku, Japan) measurements were conducted to analyse the crystalline structure of the LM and SF-coated textiles. The measurements were performed in the 2θ range of $5°$ to $100°$ with a step size of $0.02°$ and a scanning speed of $3°$ min^{-1}. Peak detection was carried out using Profex 5.4.1, followed by phase identification and matching using QualX software.

4.4. Passivation methods

Two passivation methods were developed to protect the circuits within the smart textile. For a fully protected circuit, the circuit-designed textile was blade-coated with PDMS and cured at 80 °C after resting for 4 hours at room temperature. This method completely encapsulated the circuit, preventing any further modification while enabling LM sintering. For a semi-protected circuit with modification potential, the circuit-designed textile was passivated with PDMS without a resting period before curing. This allowed for partial protection of the circuit while retaining the potential for further circuit modifications under high pressure.

4.4. Measurement of electrical properties

The electrical properties of the LM circuit on the smart textile were assessed using a USB data acquisition device (USB-6002, National Instruments) and LabVIEW system (NI PXI-4071, National Instruments). A universal tensile testing machine (Model 5969, Instron) was utilized to adjust indentation depth. Conductance was measured across various depths, rod diameters, and pressure levels to understand conductivity behavior and fabrication process variations. These experiments provided crucial insights into circuit performance and optimization for practical applications.

4.5. Functional wristband fabrication

The wrist LED indicator was fabricated by integrating components such as a power source and magnet button connectors onto the smart textile (TX 1109, Texwipe, USA) using silver epoxy (8331D, MG chemicals, Canada). A protective layer of polydimethylsiloxane (PDMS) was then uniformly applied to safeguard the internal circuitry. Additionally, attachable indicators with disconnected LEDs were prepared and coated with a semi-protective layer of PDMS. These indicators were seamlessly attached to the wristband, allowing users to easily connect the circuit using a sharp tool when needed. Through this methodical process, a versatile and functional wrist LED indicator was achieved, showcasing its potential for diverse applications in wearable technology.

4.6. Teddy bear cloth fabrication

Utilizing our circuit-designable smart textile, we crafted a reversible teddy bear cloth with unique functions on each side. One side features an LED activated in darkness, while the other side serves as a heating cloth when buttoned up. All the electrical components and magnet button connectors were attached using silver epoxy (8331D, MG chemicals, Canada). A simple color spray was applied, followed by sufficient drying time to ensure proper adherence. Despite crossed circuits, insulation ensures independent functionality. This innovation demonstrates the textile's versatility for novel applications in wearable technology.

4.7. DIY heating glove

The DIY heating glove was created by integrating electronic components onto a cotton spandex glove (DISUPPO, Canada). Components were securely attached using silver epoxy (8331D, MG chemicals, Canada), allowing for independent operation of three heating sections. The microcontroller unit (ESP32-S2, Adafruit) regulated current flow to the transistors (NSS20201LT1G, Onsemi) and controlled the heating sections. Extensive testing validated the glove's functionality, showcasing its potential for customizable heating solutions.

Author contributions

C. J. conducted the overall experiments and data analysis, contributed to the refinement of the research concept, and wrote the manuscript. K. Y. K. proposed the initial idea and performed the preliminary experiments. D. W. was responsible for imaging and figure preparation for the manuscript. Y. F. designed the application circuit and remote system. Y. Y. conducted the early-stage experiments. S. G. L. performed SEM measurements and image analysis. B. K. contributed to the improvement of the conceptual framework. L. Y. proposed application ideas. T. K. and C. M. supervised the research, provided critical feedback and revisions to the manuscript, and secured funding. All authors participated in the discussion and revision of the manuscript.

Data availability

The data supporting this article have been included as part of the ESI.†

Conflicts of interest

There are no conflicts to declare.

Acknowledgements

References

1 Y. Khan, M. Garg, Q. Gui, M. Schadt, A. Gaikwad, D. Han, N. A. Yamamoto, P. Hart, R. Welte and W. Wilson, *Adv. Funct. Mater.*, 2016, **26**, 8764–8775.

2 J. Kim, B.-Y. Kim, S. D. Park, J.-H. Seo, C.-J. Lee, M. J. Yoo and Y. Kim, *Micromachines*, 2021, **12**, 943.

3 J. Tan, F. Xie, J. Huang, H. Li, X. Liu, C. Zhao, J. Yuan and Y. Liu, *J. Mater. Sci.*, 2023, **58**, 16855–16867.

4 Y. Luo, M. R. Abidian, J.-H. Ahn, D. Akinwande, A. M. Andrews, A. Antonietti, Z. Bao, M. Berggren, C. A. Berkey and C. J. Bettinger, *ACS Nano*, 2023, **17**, 5211–5295.

5 D. Zhong, C. Wu, Y. Jiang, Y. Yuan, M.-G. Kim, Y. Nishio, C.-C. Shih, W. Wang, J.-C. Lai and X. Ji, *Nature*, 2024, **627**, 313–320.

6 Y. Liu, S. Jia, C. K. Yiu, W. Park, Z. Chen, J. Nan, X. Huang, H. Chen, W. Li and Y. Gao, *Nat. Commun.*, 2024, **15**, 4474.

7 L. Paternò and L. Lorenzon, *Front. Robot. AI*, 2023, **10**, 1075634.

8 M. Seçkin, A. Ç. Seçkin and Ç. Gençer, *Biomed. Mater. Devices*, 2023, **1**, 443–455.

9 M. M. H. Shuvo, T. Titirsha, N. Amin and S. K. Islam, *Energies*, 2022, **15**, 7495.

10 B. Park, C. Jeong, J. Ok and T.-I. Kim, *Chem. Rev.*, 2024, **124**, 6148–6197.

11 J. Jones, S. P. Lacour, S. Wagner and Z. Suo, *J. Vac. Sci. Technol., A*, 2004, **22**, 1723–1725.

12 D.-H. Kim, J. Song, W. M. Choi, H.-S. Kim, R.-H. Kim, Z. Liu, Y. Y. Huang, K.-C. Hwang, Y.-W. Zhang and J. A. Rogers, *Proc. Natl. Acad. Sci. U. S. A.*, 2008, **105**, 18675–18680.

13 B. M. Li, I. Kim, Y. Zhou, A. C. Mills, T. J. Flewwellin and J. S. Jur, *Adv. Mater. Technol.*, 2019, **4**, 1900511.

14 K. Xu, Y. Lu, S. Honda, T. Arie, S. Akita and K. Takei, *J. Mater. Chem. C*, 2019, **7**, 9609–9617.

15 H. Choi, Y. Luo, G. Olson, P. Won, J. H. Shin, J. Ok, Y. J. Yang, T. I. Kim and C. Majidi, *Adv. Funct. Mater.*, 2023, **33**, 2301388.

16 K. Y. Kwon, S. Cheeseman, A. Frias-De-Diego, H. Hong, J. Yang, W. Jung, H. Yin, B. J. Murdoch, F. Scholle and N. Crook, *Adv. Mater.*, 2021, **33**, 2104298.

17 G. Wang, C. Hou and H. Wang, *Flexible and Wearable Electronics for Smart Clothing*, Wiley-VCH, Weinheim, 2020.

18 J. Yang, P. Nithyanandam, S. Kanetkar, K. Y. Kwon, J. Ma, S. Im, J. H. Oh, M. Shamsi, M. Wilkins and M. Daniele, *Adv. Mater. Technol.*, 2023, **8**, 2202183.

19 L. Sanchez-Botero, A. Agrawala and R. Kramer-Bottiglio, *Adv. Mater. Technol.*, 2023, **8**, 2300378.

20 G. S. Jeong, D.-H. Baek, H. C. Jung, J. H. Song, J. H. Moon, S. W. Hong, I. Y. Kim and S.-H. Lee, *Nat. Commun.*, 2012, **3**, 977.

21 P. Pan, Z. Bian, X. Song and X. Zhou, *J. Appl. Mech.*, 2020, **87**, 101009.

22 S. Cai, F. M. Allioux, J. Tang, J. Han, J. Zhang, Y. He, S. Merhebi, M. J. Christoe, M. Mayyas and E. H. Wong, *Adv. Mater. Technol.*, 2022, **7**, 2101500.

23 S. M. Curtis, J. L. Gugat, L. Bumke, D. Dengiz, L. Seigner, D. Schmadel, N. S. Lazarus and E. Quandt, *Shape Mem. Superelast.*, 2023, **9**, 35–49.

24 Y. Huang, Y. Su and S. Jiang, *Flexible Electronics: Theory and Method of Structural Design*, Springer, 2023, pp. 199–228.

25 C. Majidi, K. Alizadeh, Y. Ohm, A. Silva and M. Tavakoli, *Flex. Print. Electron.*, 2022, **7**, 013002.

26 M. J. Ford, D. K. Patel, C. Pan, S. Bergbreiter and C. Majidi, *Adv. Mater.*, 2020, **32**, 2002929.

27 A. Hajalilou, A. F. Silva, P. A. Lopes, E. Parvini, C. Majidi and M. Tavakoli, *Adv. Mater. Interfaces*, 2022, **9**, 2101913.

28 Y.-H. Suh, D.-W. Shin and Y. T. Chun, *RSC Adv.*, 2019, **9**, 38085–38104.

29 T. Sakorikar, N. Mihaliak, F. Krisnadi, J. Ma, T.-I. Kim, M. Kong, O. Awartani and M. D. Dickey, *Chem. Rev.*, 2024, **124**, 860–888.

30 D. A. Kwon, S. Lee, C. Y. Kim, I. Kang, S. Park and J.-W. Jeong, *Sci. Adv.*, 2024, **10**, eadn1186.

31 R. Guo, T. Li, C. Jiang, H. Zong, X. Li, C. Wan, H. Yu and X. Huang, *Adv. Fiber Mater.*, 2024, **6**, 354–366.

32 S. Ling, X. Tian, Q. Zeng, Z. Qin, S. A. Kurt, Y. J. Tan, J. Y. Fuh, Z. Liu, M. D. Dickey, J. S. Ho and B. C. K. Tee, *Nat. Electron.*, 2024, **7**, 671–683.

33 Y.-G. Park, Y. W. Kwon, C. S. Koh, E. Kim, D. H. Lee, S. Kim, J. Mun, Y.-M. Hong, S. Lee and J.-Y. Kim, *Nat. Commun.*, 2024, **15**, 1772.

34 W. Jung, M. H. Vong, K. Kwon, J. U. Kim, S. J. Kwon, T. Kim and M. D. Dickey, *Adv. Mater.*, 2024, **36**, 2406783.

35 W. Jung, G. R. Koirala, J. S. Lee, J. U. Kim, B. Park, Y. J. Jo, C. Jeong, H. Hong, K. Kwon, Y.-S. Ye, J. Kim, K. Lee and T.-I. Kim, *ACS Nano*, 2022, **16**, 21471–21481.

36 K. Lee, P. G. Taylor, A. A. Zakhidov, H. H. Fong, H. S. Hwang, M. Chatzichristidi, G. G. Malliaras and C. K. Ober, *J. Photopolym. Sci. Technol.*, 2009, **22**, 565–569.

37 V. Vallem, V. Aggarwal and M. D. Dickey, *Adv. Mater. Technol.*, 2023, **8**, 2201233.

38 F.-M. Allioux, M. B. Ghasemian, W. Xie, A. P. O'Mullane, T. Daeneke, M. D. Dickey and K. Kalantar-Zadeh, *Nanoscale Horiz.*, 2022, **7**, 141–167.

39 L. Johnston, J. Yang, J. Han, K. Kalantar-Zadeh and J. Tang, *Mater. Chem. C*, 2022, **10**, 921–931.

40 J. Ma, F. Krisnadi, M. H. Vong, M. Kong, O. M. Awartani and M. D. Dickey, *Adv. Mater.*, 2023, **35**, 2205196.

41 M. Reis Carneiro, C. Majidi and M. Tavakoli, *Adv. Funct. Mater.*, 2023, **33**, 2306453.

42 W. G. Chung, E. Kim, Y. W. Kwon, J. Lee, S. Lee, I. Jeong and J. U. Park, *Adv. Funct. Mater.*, 2023, **34**, 307990.

43 S. Eristoff, A. M. Nasab, X. Huang and R. Kramer-Bottiglio, *Adv. Funct. Mater.*, 2023, **34**, 2309529.

44 C. Jiang, T. Li, X. Huang and R. Guo, *ACS Appl. Mater. Interfaces*, 2023, **15**, 51958–51970.

45 F. C. Liang and B. C. Tee, *Adv. Funct. Mater.*, 2024, **34**, 2400284.

46 D. Corzo, G. Tostado-Blázquez and D. Baran, *Front. Electron.*, 2020, **1**, 594003.

47 G.-H. Lee, D. H. Lee, W. Jeon, J. Yoon, K. Ahn, K. S. Nam, M. Kim, J. K. Kim, Y. H. Koo and J. Joo, *Nat. Commun.*, 2023, **14**, 4173.

48 B. Ping, Z. Zhang, Q. Liu, M. Li, Q. Yang and R. Guo, *Biosensors*, 2023, **13**, 715.

49 S. Kim, S. Kim, K. Hong, M. D. Dickey and S. Park, *ACS Appl. Mater. Interfaces*, 2022, **14**, 37110–37119.

50 X. Li, K. Hou, D. Hao, Y. Long and K. Song, *J. Mater. Chem. C*, 2023, **11**, 15008–15015.

51 M. Tavakoli, M. H. Malakooti, H. Paisana, Y. Ohm, D. Green Marques, P. Alhais Lopes, A. P. Piedade, A. T. De Almeida and C. Majidi, *Adv. Mater.*, 2018, **30**, 1801852.

52 S. Zheng, X. Wang, W. Li, Z. Liu, Q. Li and F. Yan, *Nat. Electron.*, 2024, **7**, 576–585.

53 H. Zhu, S. Wang, M. Zhang, T. Li, G. Hu and D. Kong, *npj Flex. Electron.*, 2021, **5**, 25.

54 W. Lee, H. Kim, I. Kang, H. Park, J. Jung, H. Lee, H. Park, J. S. Park, J. M. Yuk and S. Ryu, *Science*, 2022, **378**, 637–641.

55 W. Zu, H. E. Carranza and M. D. Bartlett, *ACS Appl. Mater. Interfaces*, 2024, **16**, 23895–23903.

56 P. Won, S. Coyle, S. H. Ko, D. Quinn, K. J. Hsia, P. LeDuc and C. Majidi, *Adv. Healthcare Mater.*, 2023, **12**, 2202430.